ACS APPLIED MATERIALS & INTERFACES

www.acsami.org Research Article

Highly Crystalline Mesoporous Titania Loaded with Monodispersed Gold Nanoparticles: Controllable Metal–Support Interaction in Porous Materials

Lei Jin, Ben Liu, Michael E. Louis, Gonghu Li,* and Jie He*

Cite This: ACS Appl. Mater. Interfaces 2020, 12, 9617–9627 Read Online

ACCESS | Metrics & More | Article Recommendations | Supporting Information

ABSTRACT: We report the syntheses of mesoporous Au/TiO_2 hybrid photocatalysts with ordered and crystalline frameworks using co-assembly of organosilane-containing colloidal amphiphile micelles (CAMs) and poly(ethylene oxide)-modified gold nanoparticles (AuNPs) as templates. The assembled CAMs can convert to inorganic silica during calcination at elevated temperatures, providing extraordinary thermal stability to preserve the porosity of TiO_2 and the nanostructures of AuNPs. Well-defined AuNPs supported within mesoporous TiO_2 (Au@mTiO_2) can be prepared using thermal annealing at temperatures up to 800 °C. High-temperature treatment (≥500 °C) under air is found to not only improve the crystallinity of TiO_2 but also induce oxidative strong metal–support interactions (SMSIs) at Au/TiO_2 interfaces. For oxidative SMSIs, the surface oxidation of AuNPs can generate positively charged $Au^{\delta+}$ species, while TiO_2 gets reduced simultaneously. Using photocatalytic oxidation of benzyl alcohol as a model reaction, Au@mTiO_2 calcined at 600 °C for 12 h exhibited the best activity under UV irradiation, while Au@mTiO_2 calcined at 600 °C for 2 h showed the best activity under visible light. The delicate balance between the crystallinity and porosity of TiO_2 and the SMSIs at Au–TiO_2 interfaces is found to impact the photocatalytic activity of these hybrid materials.

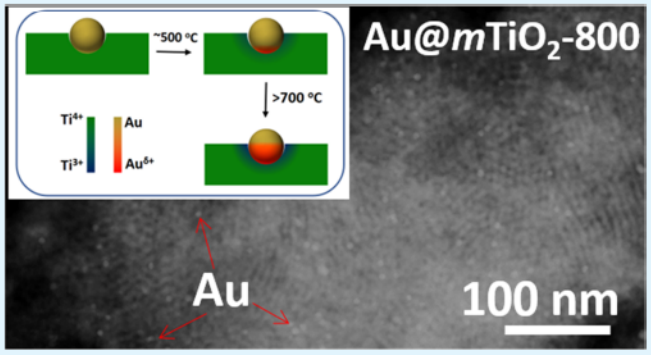

KEYWORDS: *mesoporous materials, crystalline oxides, titanium dioxide, photocatalysis, metal–support interaction, benzyl alcohol oxidation*

1. INTRODUCTION

Gold (Au) nanocatalysts supported on oxides are of broad interest in heterogeneous catalysis to mediate various chemical transformations, including CO oxidation,[1−4] water–gas shift,[5,6] alcohol oxidation,[7,8] and selective hydrogenation.[9,10] Oxide supports have proven to play a critical role in controlling the thermal stability and the catalytic activity of supported Au nanoparticles (AuNPs).[4,11,12] Among many oxides, inexpensive and photocatalytically active titania (TiO_2) has been used extensively to support AuNPs in previous literature studies.[3,8−10,13,14] Au/TiO_2 catalysts can be prepared by physical adsorption of presynthesized AuNPs,[15,16] deposition–precipitation on TiO_2 substrates,[3,13] and encapsulation of AuNPs in well-resolved nanostructures such as core–shell,[17,18] yolk–shell,[19,20] and Janus-type.[21] As supports of noble metal nanocatalysts, mesoporous materials are superior in terms of their mesoscale porosity (pore diameter 2–50 nm), which offers large surface areas and enhanced mass transport of substrates. Enhanced photocatalytic activity has been documented previously using mesoporous TiO_2 as a support for AuNPs.[22]

Unlike many redox-active oxides, for example, Fe_2O_3,[1,2] CeO_2,[7] and MnO_2,[2,23] the electronic interaction between Au and TiO_2 is rather poor as a result of weak charge transfer.[24] As such, AuNPs supported on TiO_2 always suffer from aggregation and sintering at elevated temperatures.[12,25] The formation of strong metal–support interactions (SMSIs) between Au and TiO_2 becomes critical in control of not only their catalytic activities but also the stability of AuNPs to increase the lifetime of these expensive noble metal nanocatalysts.[25−27] Dai and co-workers recently reported the use of a sacrificial carbon layer to stabilize AuNPs supported on TiO_2, while increasing temperature to enhance metal–support interactions between Au and TiO_2.[28] They showed that the formation of SMSIs at the interfaces of Au/TiO_2 could largely enhance the thermal stability of AuNPs and prolong the lifetime of Au nanocatalysts.

Received: November 7, 2019
Accepted: January 31, 2020
Published: January 31, 2020

https://dx.doi.org/10.1021/acsami.9b20231
ACS Appl. Mater. Interfaces 2020, 12, 9617–9627

Our group recently demonstrated the synthesis of thermally stable mesoporous oxides with highly crystalline walls using organosilane-containing colloidal amphiphile micelles (CAMs) as templates.[29,30] CAM templates made through micellization of poly(ethylene oxide)-*block*-poly(3-(trimethoxysilyl)propyl methacrylate) (PEO-*b*-PTMSPMA)[29,30] can convert to inorganic silica. Unlike hydrocarbon-based polymer templates, CAMs have significantly better thermal stability under air, and they can therefore acts as a template for the growth of mesoporous oxides with highly crystalline walls. When co-assembling with polymer-modified AuNPs,[31,32] presynthesized AuNPs with well-defined sizes could be encapsulated into mesoporous oxides. Because SMSIs in Au/TiO_2 are thermodynamically unfavorable at low temperature,[24] we can use thermally stable CAMs as templates to prepare well-defined AuNPs supported within mesoporous TiO_2 (Au@mTiO_2). Given the thermal stability of CAMs, these hybrid catalysts allow to control the SMSIs at the interfaces of Au/TiO_2 under high-temperature annealing, while preserving the porosity of TiO_2 and the nanostructure of AuNPs. In this study, oxidative SMSIs are found when the thermal treatment temperature of Au@mTiO_2 is higher than 500 °C. The effect of the oxidative SMSIs of Au/TiO_2 on its photocatalytic activity has been investigated using photocatalytic oxidation of benzyl alcohol as a model reaction. We expect that our results will provide a general guideline to design metal oxide hybrid catalysts with oxidative SMSIs as a means to explore their roles in heterogeneous photocatalysis.

2. EXPERIMENTAL SECTION

2.1. Materials. Hydrogen tetrachloroaurate(III) trihydrate ($HAuCl_4{\cdot}3H_2O$, >99%), trisodium citrate, titanium(IV) chloride ($TiCl_4$), titanium isopropoxide (TIPO), monomethoxy poly(ethylene oxide) (PEO_{45}-OH, $M_n \approx 2000$; PEO_{114}-OH, $M_n \approx 5{,}000$), *N,N,N′,N″,N‴*-pentamethyldiethylenetriamine (PMDETA) (>99%), 3-mercaptopropionic acid (3-MPA), *N,N′*-dicyclohexylcarbodiimide (DCC), 4-(dimethylamino)pyridine, 2-bromoisobutyryl bromide, copper(I) bromide (CuBr), triethylamine (TEA), 3-(trimethoxysilyl)-propyl methacrylate (TMSPMA), anisole, dichloromethane (CH_2Cl_2), hexane, and ethanol were purchased from Sigma-Aldrich and used without further purification unless otherwise noted. Styrene (99%) was passed through a basic aluminum oxide column prior to use. Deionized water (High-Q, Inc. 103S Stills) with a resistivity of >10.0 MΩ was used in all experiments.

2.2. Synthesis of Amphiphilic Block Copolymers of PEO-*b*-PTMSPMA. Thermally stable BCP of PEO-*b*-PTMSPMA was prepared via atom transfer radical polymerization according to the reported procedure.[29,30,33] The macroinitiator of PEO_{114}-Br was first synthesized according to the reported procedure.[34] In a typical synthesis, CuBr (116 mg, 0.8 mmol), TMSPMA (20 g, 80.6 mmol), PEO_{114}-Br (2 g, 0.4 mmol), PMDETA (0.334 mL, 1.6 mmol), and anisole (16 mL) were mixed into a 100 mL flask. The reaction mixture was degassed by three freeze−pump−thaw cycles and then filled with N_2. The flask was then placed in a preheated oil bath at 65 °C for 90 min. After polymerization, the reaction was stopped by cooling the reaction mixture to room temperature. The mixture was then diluted with dichloromethane (DCM) and passed through a SiO_2 column to remove the catalysts. The polymer solution was then concentrated and precipitated in *n*-hexane two times. $M_{n,NMR}$ estimated from ^{1}H NMR was 60.4 kg mol^{-1}. The repeating unit of PTMSPMA was calculated to be 223 using the PEO_{114} block as the internal standard, yielding the BCP of PEO_{114}-*b*-$PTMSPMA_{223}$.

2.3. Synthesis of Thermally Stable CAM Templates. The hybrid CAMs were prepared via the self-assembly of PEO_{114}-*b*-$PTMSPMA_{223}$ in a mixed solvent of ethanol and water to induce the hydrolysis/polycondensation of silane moieties in PTMSPMA blocks. In a typical experiment, 3 g of PEO-*b*-PTMSPMA was first dissolved in 100 mL of ethanol under sonication for 30 min and then stirred for 1 h at room temperature. Subsequently, 100 mL of H_2O was added dropwise into the abovementioned solution within 2 h to induce the self-assembly of BCP. After stirring for another 2 h, 2 mL of trimethylamine was added to the abovementioned solution and kept stirring for 24 h to hydrolyze the PTMSPMA cores. Lastly, CAMs were then dialyzed against ethanol for 3 h to remove water and TEA. The final concentration of BCP micelles in ethanol was controlled to be ∼15 mg mL^{-1}.

2.4. Synthesis and Surface Modification of AuNPs. AuNPs with an average diameter of 14 nm (Au_{14}) were prepared using the sodium citrate reduction method.[31,35] In a typical synthesis, 100 mg of $HAuCl_4{\cdot}3H_2O$ was first dissolved in 0.5 L of water and heated to boiling under stirring. Sodium citrate solution (30 mL, 1 wt %) was injected into the abovementioned solution and further refluxed for 30 min. The surface modifications of AuNPs were performed as reported elsewhere.[31] Typically, 200 mL of the as-made AuNPs solution was first concentrated using centrifugation and then added to 10 mL of PEO-SH aqueous solution (1 mg mL^{-1}) under vigorous stirring. The mixture solution was then stirred overnight to allow the ligand exchange. The modified AuNPs were purified by centrifugation and then dispersed in ethanol at a concentration of 1 mg mL^{-1}.

2.5. Synthesis of Au@mTiO_2. Au@mTiO_2 was synthesized using a co-template-directed method by an evaporation-induced self-assembly (EISA) approach. In the typical synthesis, 5 mL of CAM solution (15 mg mL^{-1}) was mixed with 40 μL of $TiCl_4$ and 270 μL of TIPO, followed by adding 1 mL of Au-PEO solution (1 mg mL^{-1}). Following further stirring for 1 h, the obtained homogeneous solution was poured into a Petri dish to evaporate ethanol at 40 °C for 24 h and then at 100 °C for 12 h to completely evaporate the residual solvent. The as-made hybrids were further calcined at different temperatures for 2 h with a ramp of 2 °C min^{-1} to crystallize the mesoporous framework. As a comparison, pure mTiO_2 was synthesized using the same procedures without the addition of Au-PEO.

2.6. Photocatalytic Oxidation of Benzyl Alcohol. The benzyl alcohol oxidation was tested under visible light (500−600 nm) and ultraviolet light (320−390 nm) irradiation using an OmniCure S1500 (200 Watt mercury Arc). In a typical BAOR, 260 μL of benzyl alcohol was added to a mixture of 10 mg of photocatalysts and 5 mL of toluene in a 25 mL flask under dark conditions. O_2 was bubbled into the abovementioned solution at a flow rate of 100 mL min^{-1}. After being stirred for 5 min, the UV or visible light was irradiated to start the oxidation reaction. During the reaction, 20 μL of the solution was collected every hour for GC−MS measurements. The GC−MS analysis was performed on an Agilent 7820A GC system connected with a mass spectrometer of 5975 series MSD from Agilent Technologies, and a nonpolar cross-linked methyl siloxane column with dimensions of 12 in. × 0.20 mm × 0.33 μm was used. The column starting temperature was 40 °C and then ramped at 8 °C min^{-1} to an ending temperature of 270 °C. The catalytic performance was also cross-examined using proton nuclear magnetic resonance (^{1}H NMR) with 1,4-dioxane as an internal standard.

2.7. Characterization. Transmission electron microscopy (TEM) and high-resolution TEM (HRTEM) studies were carried out using a JEOL 2010 transmission electron microscope with an accelerating voltage of 200 kV. Scanning TEM (STEM) mapping and high-angle annular dark-field STEM (HAADF−STEM) were performed using a Talos F200X atomic resolution analytical microscope. TEM and STEM samples were prepared by casting the suspension of the samples on a carbon-coated copper grid (300 mesh). The X-ray diffraction (XRD) patterns were collected on a Rigaku Ultima IV diffractometer (Cu Kα radiation, λ = 0.15406 nm) with an operating voltage of 40 kV and an operating current of 44 mA. X-ray photoelectron spectroscopy (XPS) surface analyses were performed on a PHI model 590 spectrometer with multiprobes (Physical Electronics Industries Inc.) using Al Kα radiation (λ = 1486.6 eV) as the radiation source. Binding energies (BEs) were measured for C 1s, O 1s, N 1s, and Au 4f. The XPS spectra obtained were analyzed and

https://dx.doi.org/10.1021/acsami.9b20231
ACS Appl. Mater. Interfaces 2020, 12, 9617−9627

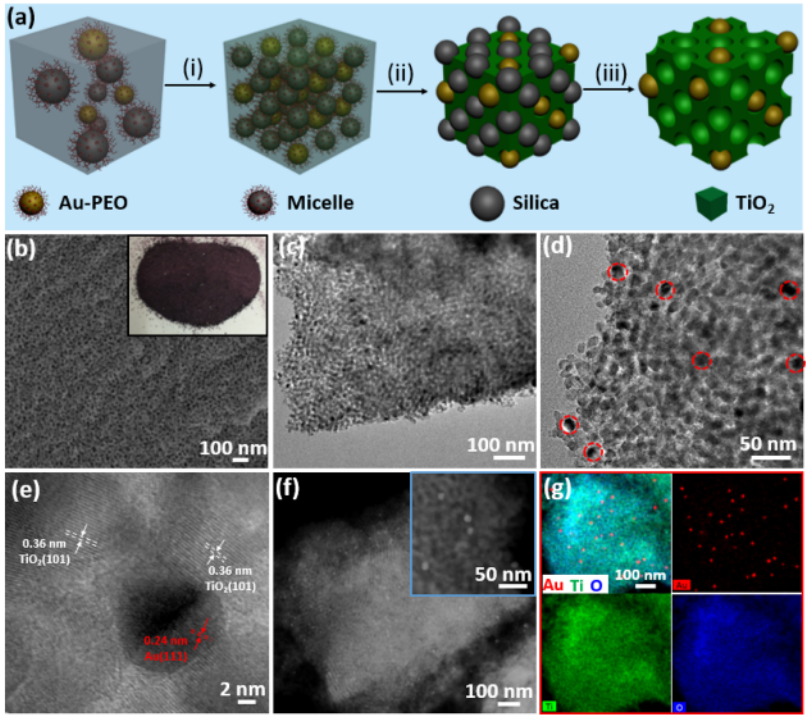

Figure 1. Synthesis and structural characterization of Au@mTiO$_2$-800. (a) Illustration showing the synthetic approach of Au@mTiO$_2$: (i) co-assembly of CAMs of PEO-*b*-PTMSPMA and Au-PEO templates in the presence of titanium sources; (ii) calcination at high temperatures to form mesoporous and crystalline TiO$_2$ frameworks; and (iii) removal of residual SiO$_2$ templates to release the pores. (b) SEM, (c,d) TEM, (e) HR-TEM, and (f) HAADF−STEM images of Au@mTiO$_2$-800. The inset in (b) is a picture of Au@mTiO$_2$-800. The dashed circles in (d) indicate AuNPs. (g) STEM−EDS mapping results of Au@mTiO$_2$-800 showing the distribution of Au (red) within Ti (green) and O (blue).

fitted using CasaXPS software (version 2.3.12). Sample charging effects were eliminated by correcting the observed spectra with a C 1s BE value of 284.6 eV. The powder samples were pressed on carbon tape, mounted on adhesive copper tape, and stuck to a sample stage placed in the analysis chamber. ^{1}H NMR spectroscopy was performed on a Bruker Avance 400 MHz spectrometer. Electron paramagnetic resonance (EPR) spectroscopy was carried out using a Bruker EMX CW microspectrometer with the perpendicular mode at room temperature. The Brunauer−Emmett−Teller (BET) surface area of catalysts was measured using a Quantachrome Autosorb-1-C-automated N$_2$ gas adsorption system. Fifty milligrams of samples were degassed at 150 °C for 12 h to remove water and other physically adsorbed species. Transient photocurrent response was measured on a CH Instrument 627E electrochemical workstation. The saturated calomel electrode and Pt wire were used as the reference electrode and counter electrode, respectively. Na$_2$SO$_4$ solution (0.1 M) was used as the electrolyte. The photocurrent response was measured under the UV light (320−390 nm) and visible light (500−600 nm) generated from a Fiber-lite series 180 illuminator with a specific filter.

3. RESULTS AND DISCUSSION

3.1. Synthesis and Structural Characterization. Au@mTiO$_2$ hybrids were synthesized via the co-assembly of CAMs and AuNPs using EISA (Figure 1a). CAMs were prepared through the self-assembly of PEO$_{114}$-*b*-PTMSPMA$_{236}$ (Figure S1) in a water/ethanol mixture (1:1, vol),[29,36] followed by dialysis against ethanol prior to use. AuNPs were synthesized via wet-chemical reduction with sodium citrate as reported previously.[37] Modification of AuNPs with thiol-terminated poly(ethylene oxide) (PEO$_{45}$-SH, molecular weight 2000 g mol^{-1}) was carried out in water through ligand exchange.[38,39] PEO-modified AuNPs (Au-PEO) have similar core−shell structures and dimension as CAMs templates,[40] which ensure the co-assembly of CAMs of Au-PEO and PEO-*b*-PTMSPMA. In addition, the PEO corona of AuNPs provide the colloidal stability in various solvents, for example, ethanol or water in the presence of metal salts. In a typical synthesis of Au@mTiO$_2$, 5 mL of the ethanol solution of CAMs (15 mg mL^{-1}) (Figure S1) was first mixed with TiCl$_4$ (40 μL) and TIPO (270 μL), followed by adding the ethanol solution of Au-PEO (varied for different Au loading amounts) under stirring. After stirring for 1 h, the mixture solution was poured into a Petri dish and dried in an oven at 40 °C for 24 h and at 100 °C for another 12 h to complete the co-assembly and the sol−gel chemistry of titania. The as-resulted transparent, red solid was then calcined at different temperatures to produce a crystalline TiO$_2$ framework loaded with AuNPs (see the Supporting Information for experimental details). In this process, the CAMs were further converted to silica-like oxides that are thermally stable and mechanically strong. The thermal stability is necessary to maintain the mesoporosity while forming the SMSIs without the collapse of pores.[41] Au@mTiO$_2$ catalysts with controllable SMSIs were achieved via varying the calcination temperatures and calcination times. All samples were denoted as Au@mTiO$_2$-*T*, where *T* is the calcination temperature.

Taking Au@mTiO$_2$-800 as an example, we characterized its porous structures and the distribution of AuNPs using electron microscopy (Figure 1b−g). Uniform mesoporous structures can be seen from low-magnification scanning electron microscopy (SEM) and TEM images in Figure 1b,c. The average size of the mesopores is around 13.6 nm (Figure S2). Aggregation-free AuNPs were well-dispersed in the mesoporous frameworks (Figure 1c−g). The powder sample of Au@mTiO$_2$-800, different from Au supported on mesoporous

https://dx.doi.org/10.1021/acsami.9b20231
ACS Appl. Mater. Interfaces 2020, 12, 9617−9627

silica[31] appeared to be dark brown that was attributed to the metal–oxide interaction. The HR-TEM image showed the crystal facets of AuNPs and TiO_2 frameworks (Figure 1e). The *d*-spacings of 0.24 and 0.36 nm were originated from the (111) facet of cubic Au and the (101) facet of anatase TiO_2, respectively. The mesoporous structures with well-dispersed AuNPs were further supported by the HAADF–STEM image, as shown in Figure 1f. AuNPs having a brighter contrast were homogeneously embedded into the mesoporous frameworks of TiO_2. The size of AuNPs is around 14.3 nm, comparable to that of the as-synthesized AuNPs (Figure S3). STEM energy-dispersive X-ray spectroscopy (STEM–EDS) mapping further confirmed the homogeneous dispersion of AuNPs within $mTiO_2$. The contrast of Au (red) dispersed within the elements of Ti (green) and O (blue) suggests the encapsulation of AuNPs within the $mTiO_2$ frameworks. The loading of Au was estimated to be 0.97 wt % relative to TiO_2 frameworks from STEM-EDS (Figure S4), close to the feeding amount (1 wt %). These results clearly demonstrate the successful synthesis of thermally stable AuNPs confined within mesoporous TiO_2 with crystalline walls.

The pore structures of Au@$mTiO_2$ prepared at different temperatures in the range of 350–900 °C were further compared using electron microscopy (Figure 2). When the calcination temperature is below 800 °C, ordered mesoporous structures with well-dispersed AuNPs can be seen (Figure 2a–f). The size of AuNPs shows minimum change along with temperature. The porous structures of TiO_2, however, became slightly less ordered with the increased calcination temperatures. The wall thickness of TiO_2 is approximately 9–10 nm (Figure S5). When the calcination temperature increased to 900 °C, the complete disruption of mesoporous structures was seen and AuNPs sintered to large aggregates (Figure 2g,h). The disrupted porous structures at high temperature might be caused by phase segregation of TiO_2 and the CAM templates.[29] The interfacial energy of crystalline walls and templates overcomes the mixing entropy that drives the formation of larger crystalline grains separated from templates. The thermal stability of mesoporous structures and AuNPs between 350 and 800 °C provides a good window to investigate SMSIs in Au/TiO_2, which is challenging using previously reported methods.[28,42]

The crystallinity of Au@$mTiO_2$ was further characterized by wide-angle XRD. XRD patterns of Au@$mTiO_2$ at all temperatures exhibited clear diffraction peaks from anatase TiO_2 (JCPDS 00-064-0863) (Figure 3a). The peak broadness gradually decreased with temperature, indicating the improvement of crystallinity. Meanwhile, diffraction peaks from AuNPs with the face-centered cubic phase are rather weak (Figure 3a, labeled with #). The low intensity is due to the low loading amount of AuNPs. There was a small peak at 27.5° for Au@$mTiO_2$-800 which can be assigned to the (110) facet of rutile TiO_2 (see Figure 3a as labeled with an arrow). The average grain sizes (AGSs) of TiO_2 were estimated using the Scherrer formula (Figure 3b). The AGSs of TiO_2 are small (<13 nm) overall. No obvious change on AGSs, that is, 6.8 nm for Au@$mTiO_2$-500 to 7.6 nm for Au@$mTiO_2$-600, is seen below 600 °C. There is an obvious increase of AGSs at 700 °C (10.8 nm) and 800 °C (12.5 nm), which indicates the improved crystallinity of TiO_2. We used UV–vis diffuse reflectance spectroscopy to examine the localized surface plasmon resonance (LSPR) of AuNPs, which reflects the macroscopic dispersity and uniformity of AuNPs within TiO_2. Because the

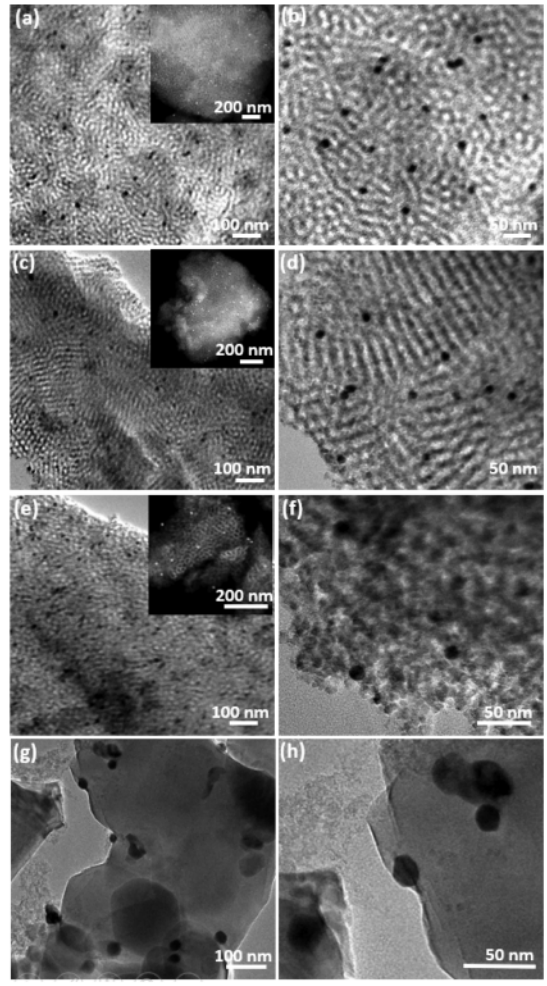

Figure 2. Structural characterization of Au@$mTiO_2$ calcined at different temperatures. TEM images of (a,b) Au@$mTiO_2$-350, (c,d) Au@$mTiO_2$-500, (e,f) Au@$mTiO_2$-600, and (g,h) Au@$mTiO_2$-900. The insets in (a,c,e) are the corresponding HAADF–STEM images.

LSPR of AuNPs is size-sensitive, it can be used to monitor the size stability of AuNPs.[43] As seen in Figure 3c, a clear LSPR peak at ~515 nm can be seen in all Au@$mTiO_2$ samples without any obvious shift. These results confirm that AuNPs are thermally stable when confined in the mesoporous $mTiO_2$ framework even at 800 °C.

Small angle X-ray scattering (SAXS) was used to confirm the ordered mesoporous structures (Figure S6). Three well-resolved scattering peaks with *q* values of 0.316, 0.611, and 0.940 nm^{-1} in Au@$mTiO_2$-600 are assigned to (111), (311), and (500) reflections, respectively, of ordered face-centered cubic mesoporous structures.[44] The average cell parameter was calculated to be 34.0 nm from the three reflections mentioned above (Table S1). The mesoporosity of Au@$mTiO_2$ was further investigated by nitrogen sorption isotherms (Figure 4). Type-IV hysteresis loops as shown in Figure 4a reveal that all Au@TiO_2 hybrids are mesoporous. The BET surface areas are 57, 77, and 70 $m^2\ g^{-1}$ for Au@$mTiO_2$-350 °C, Au@$mTiO_2$-600 °C, and Au@$mTiO_2$-800 °C, respectively. The corresponding mesopore diameters are calculated to be 14.0, 17.0, and 16.9 nm, respectively, all of which are comparable to the sizes observed in TEM (Figure 2). The slight decrease of the mesopore size is due to the shrinkage of the TiO_2 framework at relatively high temperatures.

https://dx.doi.org/10.1021/acsami.9b20231
ACS Appl. Mater. Interfaces 2020, 12, 9617–9627

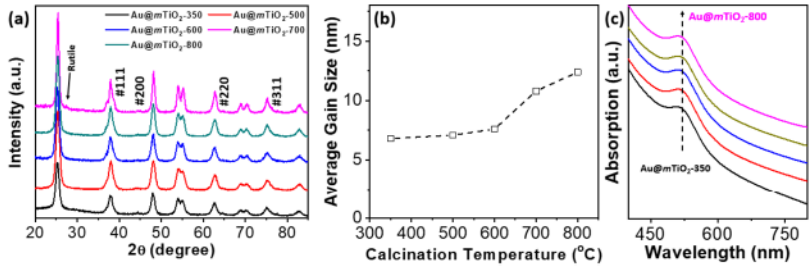

Figure 3. Structural characterization of Au@mTiO$_2$ with different calcination temperatures. (a) Wide-angle XRD patterns and (b) the corresponding average gain sizes of TiO$_2$ at different calcination temperatures. The diffraction peaks denote with # in (a) are attributed to crystalline cubic Au. (c) UV−vis spectra of Au@mTiO$_2$ with different calcination temperatures.

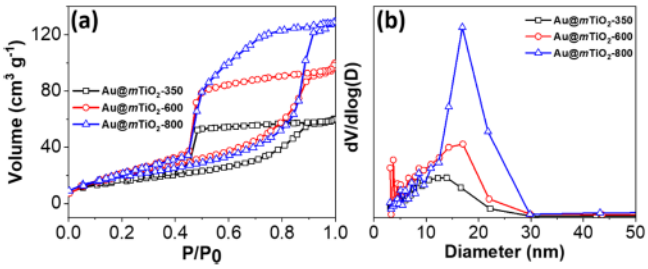

Figure 4. (a) N$_2$ sorption isotherms and (b) the corresponding pore size distribution curves of Au@mTiO$_2$-350, Au@mTiO$_2$-600, and Au@mTiO$_2$-800.

Thermal annealing for different times is another way to vary the SMSIs.[27,45] Au@mTiO$_2$ is a good candidate to study the SMSIs while maintaining the similar crystallinity and mesoporosity of TiO$_2$, given that CAM templates provide excellent thermal stability of TiO$_2$ and AuNPs. We annealed Au@mTiO$_2$ at 600 °C from 2 h to 48 h (see the Supporting Information for experimental details). As seen in Figure 5a−c, Au@mTiO$_2$-600 showed ordered mesoporous structures with uniform distribution of AuNPs regardless of the annealing time. Up to 48 h at 600 °C, the mesoporous frameworks became less ordered (Figure 5c), although AuNPs were still well-dispersed without aggregation. XRD patterns of Au@mTiO$_2$-600 showed the presence of anatase phase of TiO$_2$ (Figure 5d). When the annealing time increased to 48 h, the rutile phase of TiO$_2$ appeared. The AGSs of Au-mTiO$_2$ were also analyzed from XRD patterns (Figure 5e). No obvious change of AGSs (7.5−7.7 nm) was seen when annealing at 600 °C up to 24 h. However, when the calcination time increased to 48 h, the AGSs showed a sharp increase to 13.5 nm. The increase of AGSs is indicative of the formation of rutile TiO$_2$ that destabilizes the mesoporous frameworks as well.

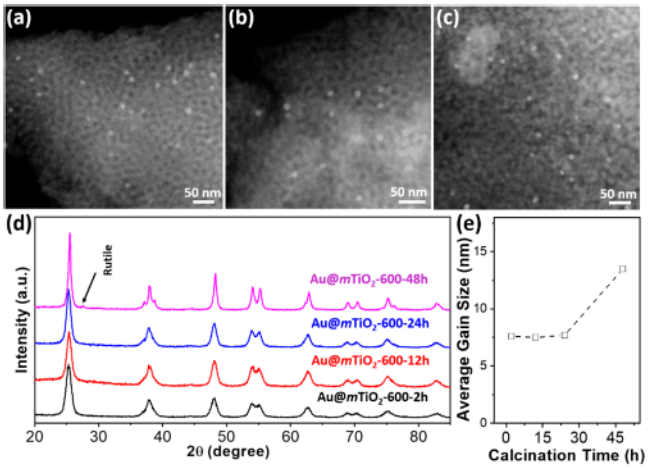

Figure 5. Structural characterization of Au@mTiO$_2$-600 with different calcination times. TEM images of (a) Au@mTiO$_2$-600-12h, (b) Au@mTiO$_2$-600-24h, and (c) Au@mTiO$_2$-600-48h. (d) Wide-angle XRD patterns and (e) corresponding AGSs of Au@mTiO$_2$-600 with different calcination times. The arrow in d indicates the rutile phase of TiO$_2$.

3.2. Photocatalytic Oxidation of Benzyl Alcohol. The photocatalytic oxidation of benzyl alcohol was used as a model reaction to evaluate the activity of Au@mTiO$_2$. The oxidation was carried out under either UV light (320−390 nm, 3 mW cm^{-2}) or visible light (500−600 nm, 13 mW cm^{-2}) at room temperature (25 °C) with O$_2$ bubbling (100 mL min^{-1}) (see the Supporting Information for experimental details). The conversion of benzyl alcohol to benzaldehyde was analyzed using ^{1}H NMR with 1,4-dioxane as an internal standard (Figure S7). For all reactions, benzaldehyde was detected as the main liquid product with a negligible amount of benzoic acid. The oxidation of toluene was proven to be minimum, compared to the oxidation of benzyl alcohol (Figure S8). The catalytic performance of Au@mTiO$_2$ was therefore summarized using the yield of benzaldehyde at a reaction time of 4 h, as given in Figure 6.

For Au@mTiO$_2$ calcined at different temperatures, the dependence of its activity on the calcination temperature followed a similar "volcano" trend (Figure 6a). Au@mTiO$_2$-350 shows the lowest activity. The yield of benzaldehyde is 1.8% under visible light and 4.3% under UV light. The improvement of crystallinity of TiO$_2$ has a positive impact on the activity. The yield of benzaldehyde using Au@mTiO$_2$-600 reaches 8.2% under UV light which is around 1.9 times more active than Au@mTiO$_2$-350. The catalytic performance was also cross-checked by the conversion of benzyl alcohol. For example, the conversion of benzyl alcohol using Au@mTiO$_2$-600 under UV light is 8.5 ± 0.8%, close to the yield of benzaldehyde (8.2 ± 1.4%). This is indicative of benzaldehyde produced solely from the oxidation of benzyl alcohol. When calcined at above 700 °C, the yield gradually decreased under both UV and visible light. The catalytic performance with a volcano plot indicated that the catalytic efficiency is not linearly correlated to the crystallinity of TiO$_2$ nor the SMSIs. The photothermal effect of AuNPs has negligible contribution to the yield of the product, as confirmed by the dark reaction performed at 50 °C (Figure S9). In addition, the catalytic performance of pure mTiO$_2$ was evaluated under UV and visible light as controls. A yield of 3.4% was shown under UV light, while no activity was shown under visible light (Figure

https://dx.doi.org/10.1021/acsami.9b20231
ACS Appl. Mater. Interfaces 2020, 12, 9617−9627

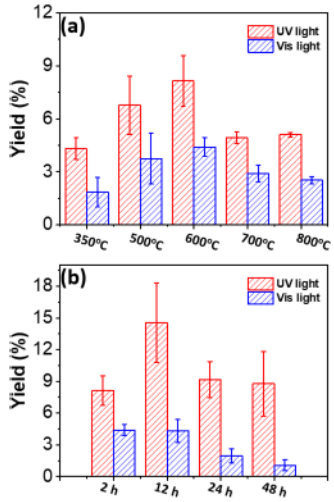

Figure 6. Photochemical oxidation of benzyl alcohol using Au@$mTiO_2$ catalysts. (a) Yield of benzaldehyde using Au@$mTiO_2$ calcined at different temperatures. (b) Yield of benzaldehyde using Au@$mTiO_2$ calcined at 600 °C for different times. Reaction conditions: catalyst: 10 mg; BA: 260 μL; toluene: 5 mL; O_2: 100 mL min^{-1}; light irradiation: UV light (320−390 nm) and visible light (500−600 nm); and reaction time: 4 h.

S10). The quantum yield of the catalyst was also evaluated at 365 nm. Au@$mTiO_2$-600 and $mTiO_2$-600 show quantum yields of 0.069 and 0.029%, respectively (see calculation details in the Supporting Information).

The catalytic stability was further evaluated by recycling the catalyst for cycles under UV and visible light (Figure S11). After five consecutive cycles, Au@$mTiO_2$-600 showed a yield retention of 85.8% and 91.3% under UV light and visible light, respectively.

We also examined the activity of Au@$mTiO_2$-600 annealed for different times (Figure 6b). A similar "volcano" trend can be seen under UV light. The highest yield of 14.5% was achieved using Au-$mTiO_2$-600-12h, which is roughly 3.4 times and 1.8 times compared to that of Au@$mTiO_2$-350 and Au@$mTiO_2$-600-2h, respectively. The activity dropped gradually with the further increase of the calcination time. Interestingly, a different trend under visible light was seen. The yield of benzaldehyde dropped gradually from 4.4% (Au-$mTiO_2$-600-2h) to 1.1% (Au-$mTiO_2$-600-48 h) under visible light.

3.3. Proposed Catalytic Mechanism. Because TiO_2 has a large band gap of 3.2 eV, its photoresponse in the visible range of 500−600 nm is minimum. UV and visible light irradiations excite semiconductors (e.g., TiO_2) and AuNPs, respectively, leading to different reaction pathways (Scheme 1). Two different mechanisms of photochemical benzyl alcohol oxidations in metal/semiconductor systems have been studied previously.[46−51] Under UV light irradiation, the band gap excitation of TiO_2 occurs. The generated holes on the valence band of TiO_2 are oxidative enough to convert surface-adsorbed benzyl alcohol to benzyl alcohol cation radicals. The excited electrons in the conduction band of TiO_2 can be separated to AuNPs across the Schottky barrier. The electrons on AuNPs can further activate O_2 to form $O_2^{\bullet-}$ anionic radicals. The $O_2^{\bullet-}$ radicals further oxidize benzyl alcohol radicals, generating benzaldehyde (Scheme 1a).

Upon irradiation by visible light, AuNPs can be excited through its LSPR (Scheme 1b).[52] The photo-excited hot electrons on AuNPs can reduce O_2 to $O_2^{\bullet-}$ species or back-transfer to the conduction band of TiO_2 to carry out oxygen reduction. The produced $O_2^{\bullet-}$ species then attract the hydrogen from benzyl alcohol, forming hydroperoxide species and alkoxide species on the surface of AuNPs.

Because of the different light irradiation and electron transfer pathways, the SMSIs likely have different effects in each case. Under oxidative thermal treatment, the oxidative SMSIs have been demonstrated in previous literature studies.[53,54] Because the Fermi level of metal oxides is lowered under oxidative treatments, this enables electronic interaction at Au-oxide interfaces.[53] This is slightly different from the classic reductive SMSIs, in which electrons normally transfer from metal oxides to metal NPs.[55−58] For example, electronic metal−support interaction between Au and TiO_2 under reductive pretreatment resulted in the electron transfer from

Scheme 1. (a) Mechanism of the Formation of Oxidative SMSIs in Au@$mTiO_2$; (b,c) Mechanism of Photocatalytic Oxidation of Benzyl Alcohol Using Au@$mTiO_2$ Under (b) UV and (c) Visible Light Irradiation

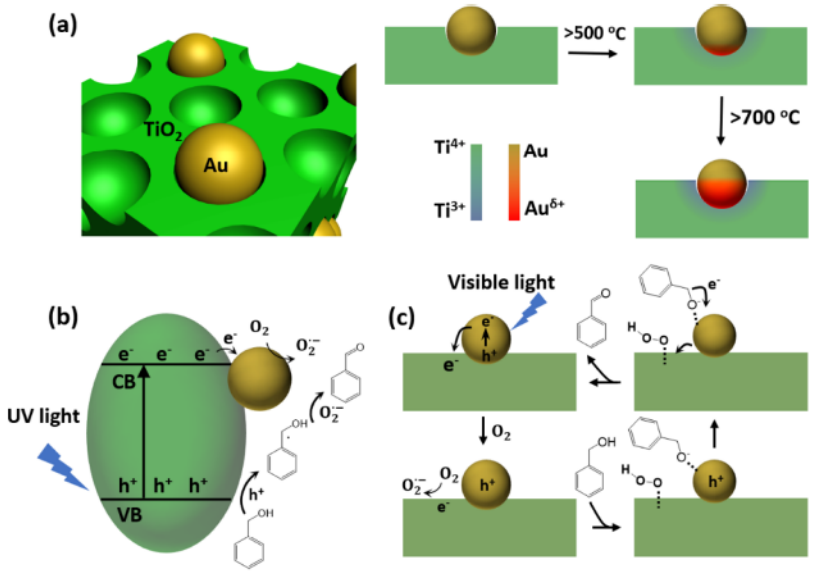

https://dx.doi.org/10.1021/acsami.9b20231
ACS Appl. Mater. Interfaces 2020, 12, 9617−9627

TiO_2 to AuNPs, leading to an electron-rich surface of AuNPs.[59] In oxidative SMSIs, the oxygen transfer is induced to oxidize the surface of metal NPs, while metal oxides get reduced simultaneously. We combined XPS, EPR, and diffuse reflectance infrared Fourier transform spectroscopy (DRIFTS) to probe the electronic interaction of AuNPs and TiO_2. The oxidative SMSIs were also proved to be temperature-dependent. It changes the physicochemical properties of catalysts (crystallinity, surface oxidation states, electron transfer, etc.) and subsequently affects the catalytic performance.

3.4. Metal–Support Interactions in Au@mTiO$_2$ Calcined at Different Temperatures. XPS was first used to characterize the oxidation states of Au and Ti in mTiO$_2$-600 and Au@mTiO$_2$-600 (Figure 7). For Ti 2p, mTiO$_2$ without

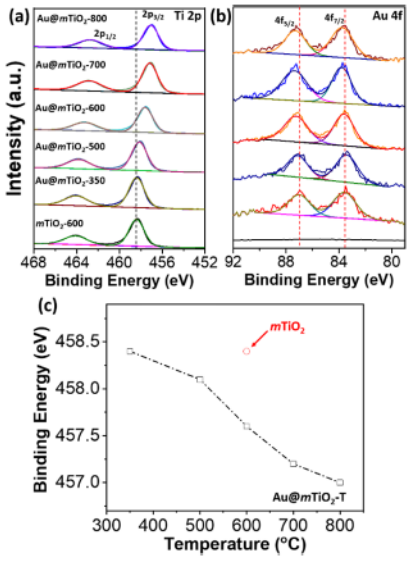

Figure 7. Electronic analysis of Au@mTiO$_2$ calcined at different temperatures. XPS spectra of (a) Ti 2p and (b) Au 4f of Au@mTiO$_2$-*T*. (c) Binding energy of Ti $2p_{3/2}$ of Au@mTiO$_2$-*T* as a function of temperature.

AuNPs (mTiO$_2$-600, Figure S12) has two split peaks at 458.4 and 464.1 eV, assigned to Ti $2p_{3/2}$ and Ti $2p_{1/2}$, respectively. The splitting of the two peaks is 5.7 eV, in close agreement with that of anatase TiO_2 reported previously.[60] An obvious peak shift of Ti 2p was observed for Au@mTiO$_2$-600. Au@mTiO$_2$-600 has the Ti $2p_{3/2}$ peak at 457.6 eV, about 0.8 eV lower than that of mTiO$_2$-600. This peak shift is indicative of the presence of Ti^{3+} species from the surface reduction. Because both samples were prepared under the identical condition, the shift of the Ti 2p peak is attributed to the SMSIs at the Au–TiO_2 interfaces.

To investigate the temperature dependence of the SMSIs, XPS spectra of Au@mTiO$_2$ calcined at different temperatures were collected (Figure 7). When the calcination temperature is low, for example, 350 °C, the binding energy of Ti 2p is identical to that of pure TiO_2. The weak SMSIs have less impact on the electronic interaction of Au–TiO_2. The binding energy of Ti 2p became lower when increasing the calcination temperature. For example, the Ti $2p_{3/2}$ shifted gradually from 458.4 eV to 457.0 eV when the calcination temperature changed from 350 to 800 °C. A nearly linear correlation between Ti $2p_{3/2}$ binding energy and the calcination temperature is observed as plotted in Figure 7c.

To further confirm the presence of SMSIs in Au@mTiO$_2$, Au 4f spectra were also collected, as given in Figure 7b. Because the loading of Au is low, the Au 4f signal-to-noise ratio is rather low even with extra scanning. The Au $4f_{7/2}$ peak at 83.6 eV was seen in Au@mTiO$_2$-350, slightly lower than that of bulk Au. This can be assigned to Au^0 species bound at oxygen vacancies (O^-) during sol–gel synthesis.[61,62] When increasing the calcination temperature, the Au $4f_{7/2}$ peak shifted to 83.8 eV gradually. It is a smaller shift compared to that of Ti 2p, given an XPS penetration depth of 5–10 nm to cover the entire AuNPs (not only on the surface). This strongly suggests the formation of oxidative $Au^{\delta+}$ species.[63,64] Together with Ti 2p results, there are SMSIs between Au and TiO_2 where the electronic perturbation appeared at Au–TiO_2 interfaces.

The SMSIs in Au@mTiO$_2$ were also revealed by EPR (Figure 8a). A clear peak at g = 2.004 can be found in the EPR

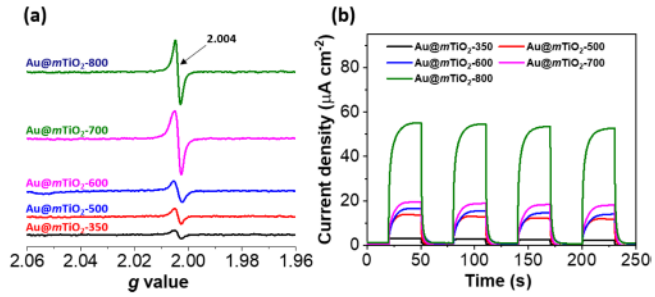

Figure 8. (a) EPR spectra of Au@mTiO$_2$-*T* collected at room temperature. (b) Photocurrent vs time (I–t) curves of Au@mTiO$_2$ at a potential of 1.23 V (vs RHE) under UV irradiation (320–390 nm).

spectra of all Au@mTiO$_2$ samples, while it is absent in the spectrum of mTiO$_2$-600 (Figure S13). This peak is assigned to electrons trapped at oxygen vacancies at Au–TiO_2 interfaces,[65] which are usually related to the electron transfer from AuNPs. When increasing the calcination temperature, the resonance peak at g = 2.004 became more pronounced. Although a quantitative comparison cannot be performed in the powder samples, the increase of the peak intensity indicates the formation of much stronger electronic interaction at Au–TiO_2 interfaces. These results are in good agreement with the XPS analysis mentioned above.

Varying calcination temperature has a significant impact not only on the SMSIs of Au@mTiO$_2$ but also on the crystallinity of mTiO$_2$ frameworks, as discussed in XRD. To identify possible contribution of the TiO_2 crystallinity on photocatalysis, we have examined the photocurrent response of Au@mTiO$_2$ (Figure 8b). Under UV irradiation, there is considerable anodic current response. The photocurrent of Au@mTiO$_2$-350 was measured to be 3.6 μA cm^{-2}. A clear trend in the photocurrent was seen when increasing the calcination temperature. The photocurrent reached 55.0 μA cm^{-2} for Au@mTiO$_2$-800. For the samples calcined at 500–700 °C, the photocurrent is very close. For anodic response, because photogenerated holes on TiO_2 are accountable for the photocurrent, improving the crystallinity of TiO_2 has largely improved the lifetime of holes, which increases the anodic photocurrent.[66] However, the photocatalytic efficiency of Au@

https://dx.doi.org/10.1021/acsami.9b20231
ACS Appl. Mater. Interfaces 2020, 12, 9617–9627

$mTiO_2$ under UV does not fully align with the photocurrent response (see Figure 6).

The oxidative SMSIs in Au@$mTiO_2$ results in the formation of $Au^{\delta+}$ species, as reported previously by Lin et al.[53] The driving force is the relative lower Fermi level of TiO_2 that allows electron transfer from AuNPs to the oxide. The XPS results shown in Figure 7 clearly confirmed the formation of Ti^{3+} and $Au^{\delta+}$ species in Au@$mTiO_2$ prepared at temperatures greater than 500 °C. Therefore, the oxidative SMSIs are present in our samples. Further increasing the temperature will lead to oxygen transfer that covers the surface of AuNPs and therefore reduces the accessibility of AuNPs. Because AuNPs separate excited electrons from the band gap excitation from TiO_2, the loss of surface accessibility will block the reductive half reaction and eventually lead to the trapping of excited electrons. As a result, the decrease in photocatalytic activity of Au@$mTiO_2$ calcined at 700 and 800 °C was observed, as shown in Figure 6.

On the other hand, the photocurrent was also obtained under visible light irradiation which excites the LSPR of AuNPs (Figure S14). A much lower photocurrent was observed. Au@$mTiO_2$-600 showed the highest photocurrent of 5.2 nA cm^{-2}, compared with that of Au@$mTiO_2$-350 (2.9 nA cm^{-2}), Au@$mTiO_2$-500 (2.9 nA cm^{-2}), Au@$mTiO_2$-700 (4.1 nA cm^{-2}), and Au@$mTiO_2$-800 (4.4 nA cm^{-2}). The photocurrent is in close agreement with the photochemical performance under visible light. Under visible light, hot holes generated on Au are responsible for the photocurrent. At low calcination temperature, the increase of photocatalytic activity of Au@$mTiO_2$ with temperature is likely due to the improvement of electron conductivity of TiO_2. When generating oxidative SMSIs, the visible light photocatalytic activity also decreased because (i) the surface coverage of AuNPs limits accessibility of the catalytic sites and (ii) $Au^{\delta+}$ species on AuNPs presumably disfavor hot electron injection as discussed below.

3.5. Metal−Support Interactions in Au@$mTiO_2$ Annealed at 600 °C. Although changing the calcination temperature has a large impact on the activity of Au@$mTiO_2$, the crystallinity of TiO_2 and the SMSIs are tightly entangled and their roles in photocatalytic activity cannot be resolved. We therefore chose to use thermal annealing at 600 °C that will have a minimum impact on crystallinity of TiO_2 (see Figure 5e) but possibly control the SMSIs. XPS again was used to probe the presence of SMSIs in Au@$mTiO_2$-600 prepared at different annealing times. The results are summarized in Figure 9. Similar but less pronounced peak shifts can be seen for Ti 2p and Au 4f when the annealing time increased from 2 h to 48 h. Au@$mTiO_2$-600-2h showed a Ti $2p_{3/2}$ peak at 457.6 eV, which shifted to 457.3 eV for Au@$mTiO_2$-600-48h. The Au 4f peaks did not display a clear peak shift with increased annealing temperature. The adsorption of CO as a probe molecule was used to probe the surface electronic state of Au (Figure S15). For Au@$mTiO_2$-600-2h, a CO peak at 2112 cm^{-1} can be seen, which is assigned to the CO bonded on atop sites of AuNPs.[67,68] With the increased calcination time, the peak gradually shifts to a high value with a broad peak appearing at 2130 cm^{-1}. The red shift in the CO peak is indicative of the formation of electron-deficient $Au^{\delta+}$ species on the surface.[67] This suggested that annealing at 600 °C could readily change the SMSIs while not significantly changing the crystallinity of TiO_2 (annealing for less than 24 h, Figure 5e).

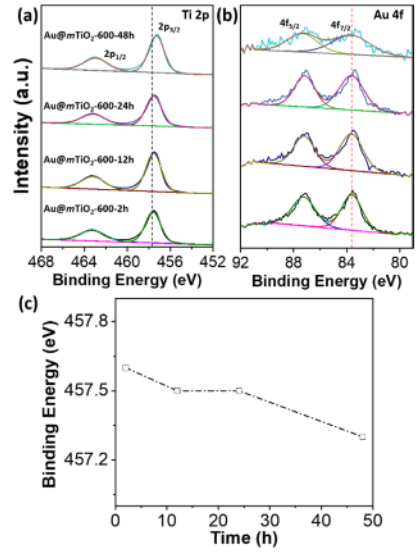

Figure 9. Electronic analysis of Au@$mTiO_2$-600 at different annealing times. XPS spectra of (a) Ti 2p and (b) Au 4f of Au@$mTiO_2$-600 with different calcination times. (c) Binding energy change of Ti $2p_{3/2}$ of Au@$mTiO_2$-*T*.

The EPR and the photocurrent of Au@$mTiO_2$-600 at different annealing times are displayed in Figure 10. The peak

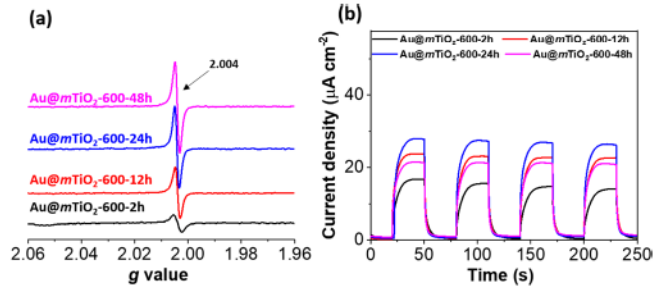

Figure 10. (a) EPR spectra of Au@$mTiO_2$-600 at different annealing times. (b) Photocurrent vs time (*I*−*t*) curves of Au@$mTiO_2$ at a potential of 1.23 V (vs RHE) under UV irradiation (320−390 nm).

at g = 2.004, again, assigned to the electron-filled oxygen vacancies, showed an obvious increase with the annealing time, indicating the formation of stronger metal−support electronic interactions. The photocurrent of Au@$mTiO_2$-600 under UV irradiation is shown in Figure 10b. Under UV light, the photocurrent increased from 16.8 μA cm^{-2} (Au@$mTiO_2$-600-2h) to 27.9 μA cm^{-2} (Au@$mTiO_2$-600-24h). The photocurrent had a slight decrease to 21.6 μA cm^{-2} for Au@$mTiO_2$-600-48h, which was likely caused by the collapse of mesoporous structures because of the formation of rutile TiO_2.[69] It is noteworthy that Au@$mTiO_2$-600-12h and Au@$mTiO_2$-700-2h show a similar photocurrent but their photoactivity is completely different. As shown in Figure 6, the activity of Au@$mTiO_2$-600-12h is roughly 2.9 times higher than that of Au@$mTiO_2$-700-2h. This result suggests that the hole generation rate of the two samples are similar (photocurrent) but the charge separation on Au@$mTiO_2$-600-12h is improved (photocatalysis). These positively charged $Au^{\delta+}$ species generated by the SMSIs contribute to photocatalysis by separating charges from TiO_2 band gap excitation. A possible explanation is that the presence of $Au^{\delta+}$ species

https://dx.doi.org/10.1021/acsami.9b20231
ACS Appl. Mater. Interfaces 2020, 12, 9617−9627

facilitates interfacial transfer of excited electrons from TiO_2, thus enhancing the catalytic performance.

The photocurrent under visible light was still low for these samples. Au@mTiO_2-600-2h showed a slightly higher photocurrent of 5.2 nA cm^{-2} than other samples. This is in close agreement with the catalytic performance of samples with different annealing times where photocatalytic activity of Au@mTiO_2-600 decreased with increasing annealing time at 600 °C. These results suggest that $Au^{\delta+}$ species are detrimental to photocatalytic activity of Au@mTiO_2 when exciting the LSPR of AuNPs. One possible reason is that the oxidized Au species trap the hot electrons to diminish the photocatalytic performance.[70]

4. CONCLUSIONS

In summary, we demonstrated a facile synthetic method to prepare Au@mTiO_2 hybrid photocatalysts with ordered, crystalline, and porous frameworks using co-assembly of CAM templates and PEO-Au NPs. The as-made Au@mTiO_2 hybrids exhibited excellent thermal stability (in terms of their porosity and the nanostructures of AuNPs) at elevated temperatures up to 800 °C. Thermal treatment was found to improve crystallinity of TiO_2 and induce oxidative SMSIs, both of which show strong effects on the catalytic performance. When calcined at 600 °C for 12 h, Au@mTiO_2 exhibited the best photoactivity under UV, roughly 3.4 times higher than that of Au@mTiO_2-350 and 1.8 times higher than that of Au@mTiO_2-600-2h. This is originated from the delicate balance between the crystallinity and the porosity of TiO_2 and the SMSIs at Au−TiO_2 interfaces. Under visible light, we found that $Au^{\delta+}$ species generated from the SMSIs of Au−TiO_2 were detrimental to photocatalytic activity of Au@mTiO_2. Because the formation of oxidative SMSIs requires high-temperature annealing under air, our synthetic method illustrates a powerful way to retain the nanostructures of AuNPs and the porosity of TiO_2. We therefore believe that our results potentially provide new insights into the role of oxidative SMSIs in heterogeneous catalysis.

■ ASSOCIATED CONTENT

Supporting Information

The Supporting Information is available free of charge at https://pubs.acs.org/doi/10.1021/acsami.9b20231.

Synthetic procedures of catalysts, additional electron microscopic images, SAXS patterns, and EPR and CO DRIFTS spectra (PDF)

■ AUTHOR INFORMATION

Corresponding Authors

Gonghu Li − *Department of Chemistry, University of New Hampshire, Durham, New Hampshire 03824, United States;* orcid.org/0000-0002-2924-3597; Email: gonghu.li@unh.edu

Jie He − *Department of Chemistry and Polymer Program, Institute of Materials Science, University of Connecticut, Storrs, Connecticut 06269, United States;* orcid.org/0000-0003-0252-3094; Email: jie.he@uconn.edu

Authors

Lei Jin − *Department of Chemistry, University of Connecticut, Storrs, Connecticut 06269, United States*

Ben Liu − *Department of Chemistry, University of Connecticut, Storrs, Connecticut 06269, United States; Jiangsu Key Laboratory of New Power Batteries, Jiangsu Collaborative Innovation Center of Biomedical Functional Materials, School of Chemistry and Materials Science, Nanjing Normal University, Nanjing 210023, China;* orcid.org/0000-0003-1305-5900

Michael E. Louis − *Department of Chemistry, University of New Hampshire, Durham, New Hampshire 03824, United States*

Complete contact information is available at: https://pubs.acs.org/10.1021/acsami.9b20231

Notes

The authors declare no competing financial interest.

■ ACKNOWLEDGMENTS

J.H. and G.L. are grateful for the financial support from the U.S. National Science Foundation, grants #CBET-1705566 and 1936228 to J.H. and grant # CBET-1705528 to G.L. J.H. also thanks the startup fund from the University of Connecticut and the Green Emulsions Micelles and Surfactants (GEMS) Center. The authors thank Dr. Clyde Cady for the help on EPR experiments. The SEM/TEM studies were performed using the facilities in the UConn/FEI Center for Advanced Microscopy and Materials Analysis (CAMMA).

■ REFERENCES

(1) Haruta, M.; Yamada, N.; Kobayashi, T.; Iijima, S. Gold Catalysts Prepared by Coprecipitation for Low-Temperature Oxidation of Hydrogen and of Carbon Monoxide. *J. Catal.* **1989**, *115*, 301−309.

(2) Haruta, M.; Kobayashi, T.; Sano, H.; Yamada, N. Novel Gold Catalysts for the Oxidation of Carbon Monoxide at a Temperature far Below 0 °C. *Chem. Lett.* **1987**, *16*, 405−408.

(3) Yan, W.; Chen, B.; Mahurin, S. M.; Schwartz, V.; Mullins, D. R.; Lupini, A. R.; Pennycook, S. J.; Dai, S.; Overbury, S. H. Preparation and Comparison of Supported Gold Nanocatalysts on Anatase, Brookite, Rutile, and P25 Polymorphs of TiO_2 for Catalytic Oxidation of CO. *J. Phys. Chem. B* **2005**, *109*, 10676−10685.

(4) Ma, G.; Binder, A.; Chi, M.; Liu, C.; Jin, R.; Jiang, D.-e.; Fan, J.; Dai, S. Stabilizing gold clusters by heterostructured transition-metal oxide-mesoporous silica supports for enhanced catalytic activities for CO oxidation. *Chem. Commun.* **2012**, *48*, 11413−11415.

(5) Fu, Q.; Weber, A.; Flytzani-Stephanopoulos, M. Nanostructured Au−CeO_2 Catalysts for Low-Temperature Water−Gas Shift. *Catal. Lett.* **2001**, *77*, 87−95.

(6) Ma, Z.; Yin, H.; Dai, S. Performance of Au/M_xO_y/TiO_2 Catalysts in Water-Gas Shift Reaction. *Catal. Lett.* **2010**, *136*, 83−91.

(7) Enache, D. I.; Knight, D. W.; Hutchings, G. J. Solvent-free Oxidation of Primary Alcohols to Aldehydes Using Supported Gold Catalysts. *Catal. Lett.* **2005**, *103*, 43−52.

(8) Enache, D. I.; Edwards, J. K.; Landon, P.; Solsona-Espriu, B.; Carley, A. F.; Herzing, A. A.; Watanabe, M.; Kiely, C. J.; Knight, D. W.; Hutchings, G. J. Solvent-Free Oxidation of Primary Alcohols to Aldehydes Using Au-Pd/TiO_2 Catalysts. *Science* **2006**, *311*, 362−365.

(9) Mohr, C.; Hofmeister, H.; Claus, P. The Influence of Real Structure of Gold Catalysts in the Partial Hydrogenation of Acrolein. *J. Catal.* **2003**, *213*, 86−94.

(10) Corma, A.; Serna, P.; García, H. Gold Catalysts Open a New General Chemoselective Route to Synthesize Oximes by Hydrogenation of α,β-Unsaturated Nitrocompounds with H_2. *J. Am. Chem. Soc.* **2007**, *129*, 6358−6359.

(11) Corma, A.; Garcia, H. Supported Gold Nanoparticles as Catalysts for Organic Reactions. *Chem. Soc. Rev.* **2008**, *37*, 2096−2126.

(12) Ta, N.; Liu, J.; Chenna, S.; Crozier, P. A.; Li, Y.; Chen, A.; Shen, W. Stabilized Gold Nanoparticles on Ceria Nanorods by Strong Interfacial Anchoring. *J. Am. Chem. Soc.* **2012**, *134*, 20585−20588.
(13) Haruta, M.; Tsubota, S.; Kobayashi, T.; Kageyama, H.; Genet, M. J.; Delmon, B. Low-Temperature Oxidation of CO over Gold Supported on TiO_2, α-Fe_2O_3, and Co_3O_4. *J. Catal.* **1993**, *144*, 175−192.
(14) Zhang, L.; Jin, L.; Liu, B.; He, J. Templated Growth of Crystalline Mesoporous Materials: From Soft/Hard Templates to Colloidal Templates. *Front. Chem.* **2019**, *7*, 22.
(15) Chandrasekharan, N.; Kamat, P. V. Improving the Photoelectrochemical Performance of Nanostructured TiO_2 Films by Adsorption of Gold Nanoparticles. *J. Phys. Chem. B* **2000**, *104*, 10851−10857.
(16) Zheng, N.; Stucky, G. D. A General Synthetic Strategy for Oxide-Supported Metal Nanoparticle Catalysts. *J. Am. Chem. Soc.* **2006**, *128*, 14278−14280.
(17) Cushing, S. K.; Li, J.; Bright, J.; Yost, B. T.; Zheng, P.; Bristow, A. D.; Wu, N. Controlling Plasmon-Induced Resonance Energy Transfer and Hot Electron Injection Processes in Metal@TiO_2 Core−Shell Nanoparticles. *J. Phys. Chem. C* **2015**, *119*, 16239−16244.
(18) Goebl, J.; Joo, J. B.; Dahl, M.; Yin, Y. Synthesis of Tailored Au@TiO_2 Core−Shell Nanoparticles for Photocatalytic Reforming of Ethanol. *Catal. Today* **2014**, *225*, 90−95.
(19) Lee, I.; Joo, J. B.; Yin, Y.; Zaera, F. A Yolk@Shell Nanoarchitecture for Au/TiO_2 Catalysts. *Angew. Chem., Int. Ed.* **2011**, *50*, 10208−10211.
(20) Li, A.; Zhang, P.; Chang, X.; Cai, W.; Wang, T.; Gong, J. Gold Nanorod@TiO_2 Yolk-Shell Nanostructures for Visible-Light-Driven Photocatalytic Oxidation of Benzyl Alcohol. *Small* **2015**, *11*, 1892−1899.
(21) Wu, B.; Liu, D.; Mubeen, S.; Chuong, T. T.; Moskovits, M.; Stucky, G. D. Anisotropic Growth of TiO_2 onto Gold Nanorods for Plasmon-Enhanced Hydrogen Production from Water Reduction. *J. Am. Chem. Soc.* **2016**, *138*, 1114−1117.
(22) Li, H.; Bian, Z.; Zhu, J.; Huo, Y.; Li, H.; Lu, Y. Mesoporous Au/TiO_2 Nanocomposites with Enhanced Photocatalytic Activity. *J. Am. Chem. Soc.* **2007**, *129*, 4538−4539.
(23) Kuo, C.-H.; Li, W.; Pahalagedara, L.; El-Sawy, A. M.; Kriz, D.; Genz, N.; Guild, C.; Ressler, T.; Suib, S. L.; He, J. Understanding the Role of Gold Nanoparticles in Enhancing the Catalytic Activity of Manganese Oxides in Water Oxidation Reactions. *Angew. Chem., Int. Ed.* **2015**, *54*, 2345−2350.
(24) Fu, Q.; Wagner, T. Interaction of Nanostructured Metal Overlayers with Oxide Surfaces. *Surf. Sci. Rep.* **2007**, *62*, 431−498.
(25) Goodman, D. W. ?Catalytically active Au on Titania:? yet another example of a strong metal support interaction (SMSI)? *Catal. Lett.* **2005**, *99*, 1−4.
(26) Murdoch, M.; Waterhouse, G. I. N.; Nadeem, M. A.; Metson, J. B.; Keane, M. A.; Howe, R. F.; Llorca, J.; Idriss, H. The Effect of Gold Loading and Particle Size on Photocatalytic Hydrogen Production from Ethanol over Au/TiO_2 Nanoparticles. *Nat. Chem.* **2011**, *3*, 489−492.
(27) Tang, H.; Su, Y.; Zhang, B.; Lee, A. F.; Isaacs, M. A.; Wilson, K.; Li, L.; Ren, Y.; Huang, J.; Haruta, M.; Qiao, B.; Liu, X.; Jin, C.; Su, D.; Wang, J.; Zhang, T. Classical strong metal-support interactions between gold nanoparticles and titanium dioxide. *Sci. Adv.* **2017**, *3*, No. e1700231.
(28) Zhan, W.; He, Q.; Liu, X.; Guo, Y.; Wang, Y.; Wang, L.; Guo, Y.; Borisevich, A. Y.; Zhang, J.; Lu, G.; Dai, S. A Sacrificial Coating Strategy Toward Enhancement of Metal-Support Interaction for Ultrastable Au Nanocatalysts. *J. Am. Chem. Soc.* **2016**, *138*, 16130−16139.
(29) Liu, B.; Luo, Z.; Federico, A.; Song, W.; Suib, S. L.; He, J. Colloidal Amphiphile-Templated Growth of Highly Crystalline Mesoporous Nonsiliceous Oxides. *Chem. Mater.* **2015**, *27*, 6173−6176.
(30) Liu, B.; Yao, H.; Daniels, R. A.; Song, W.; Zheng, H.; Jin, L.; Suib, S. L.; He, J. A facile synthesis of Fe_3C@mesoporous carbon nitride nanospheres with superior electrocatalytic activity. *Nanoscale* **2016**, *8*, 5441−5445.
(31) Liu, B.; Jiang, T.; Zheng, H.; Dissanayke, S.; Song, W.; Federico, A.; Suib, S. L.; He, J. Nanoengineering of aggregation-free and thermally-stable gold nanoparticles in mesoporous frameworks. *Nanoscale* **2017**, *9*, 6380−6390.
(32) Liu, B.; Kuo, C.-H.; Chen, J.; Luo, Z.; Thanneeru, S.; Li, W.; Song, W.; Biswas, S.; Suib, S. L.; He, J. Ligand-Assisted Co-Assembly Approach toward Mesoporous Hybrid Catalysts of Transition-Metal Oxides and Noble Metals: Photochemical Water Splitting. *Angew. Chem., Int. Ed.* **2015**, *54*, 9061−9065.
(33) Liu, B.; Jin, L.; Zheng, H.; Yao, H.; Wu, Y.; Lopes, A.; He, J. Ultrafine Co-based Nanoparticle@Mesoporous Carbon Nanospheres toward High-Performance Supercapacitors. *ACS Appl. Mater. Interfaces* **2017**, *9*, 1746−1758.
(34) Li, W.; Kuo, C.-H.; Kanyo, I.; Thanneeru, S.; He, J. Synthesis and Self-Assembly of Amphiphilic Hybrid Nano Building Blocks via Self-Collapse of Polymer Single Chains. *Macromolecules* **2014**, *47*, 5932−5941.
(35) Liu, B.; Kuo, C.-H.; Chen, J.; Luo, Z.; Thanneeru, S.; Li, W.; Song, W.; Biswas, S.; Suib, S. L.; He, J. Ligand-Assisted Co-Assembly Approach toward Mesoporous Hybrid Catalysts of Transition-Metal Oxides and Noble Metals: Photochemical Water Splitting. *Angew. Chem., Int. Ed.* **2015**, *54*, 9061−9065.
(36) Du, J.; Chen, Y. Hairy Nanospheres by Gelation of Reactive Block Copolymer Micelles. *Macromol. Rapid Commun.* **2005**, *26*, 491−494.
(37) Frens, G. Controlled Nucleation for the Regulation of the Particle Size in Monodisperse Gold Suspensions. *Nat. Phys. Sci.* **1973**, *241*, 20−22.
(38) He, J.; Liu, Y.; Babu, T.; Wei, Z.; Nie, Z. Self-Assembly of Inorganic Nanoparticle Vesicles and Tubules Driven by Tethered Linear Block Copolymers. *J. Am. Chem. Soc.* **2012**, *134*, 11342−11345.
(39) Li, W.; Kanyo, I.; Kuo, C.-H.; Thanneeru, S.; He, J. pH-Programmable Self-Assembly of Plasmonic Nanoparticles: Hydrophobic Interaction versus Electrostatic Repulsion. *Nanoscale* **2015**, *7*, 956−964.
(40) Liu, B.; Louis, M.; Jin, L.; Li, G.; He, J. Co-Template Directed Synthesis of Gold Nanoparticles in Mesoporous Titanium Dioxide. *Chem.—Eur. J.* **2018**, *24*, 9651−9657.
(41) Wang, L.-C.; He, L.; Liu, Y.-M.; Cao, Y.; He, H.-Y.; Fan, K.-N.; Zhuang, J.-H. Effect of Pretreatment Atmosphere on CO Oxidation over α-Mn_2O_3 Supported Gold Catalysts. *J. Catal.* **2009**, *264*, 145−153.
(42) Lu, J.; Fu, B.; Kung, M. C.; Xiao, G.; Elam, J. W.; Kung, H. H.; Stair, P. C. Coking- and Sintering-Resistant Palladium Catalysts Achieved Through Atomic Layer Deposition. *Science* **2012**, *335*, 1205.
(43) Orendorff, C. J.; Sau, T. K.; Murphy, C. J. Shape-Dependent Plasmon-Resonant Gold Nanoparticles. *Small* **2006**, *2*, 636−639.
(44) Zhu, Y.; Zhao, Y.; Ma, J.; Cheng, X.; Xie, J.; Xu, P.; Liu, H.; Liu, H.; Zhang, H.; Wu, M.; Elzatahry, A. A.; Alghamdi, A.; Deng, Y.; Zhao, D. Mesoporous Tungsten Oxides with Crystalline Framework for Highly Sensitive and Selective Detection of Foodborne Pathogens. *J. Am. Chem. Soc.* **2017**, *139*, 10365−10373.
(45) Tang, H.; Wei, J.; Liu, F.; Qiao, B.; Pan, X.; Li, L.; Liu, J.; Wang, J.; Zhang, T. Strong Metal-Support Interactions between Gold Nanoparticles and Nonoxides. *J. Am. Chem. Soc.* **2016**, *138*, 56−59.
(46) Kimura, K.; Naya, S.-i.; Jin-nouchi, Y.; Tada, H. TiO_2 Crystal Form-Dependence of the Au/TiO_2 Plasmon Photocatalyst's Activity. *J. Phys. Chem. C* **2012**, *116*, 7111−7117.
(47) Feng, W.; Wu, G.; Li, L.; Guan, N. Solvent-Free Selective Photocatalytic Oxidation of Benzyl Alcohol over Modified TiO_2. *Green Chem.* **2011**, *13*, 3265−3272.
(48) Yurdakal, S.; Palmisano, G.; Loddo, V.; Augugliaro, V.; Palmisano, L. Nanostructured Rutile TiO_2 for Selective Photocatalytic Oxidation of Aromatic Alcohols to Aldehydes in Water. *J. Am. Chem. Soc.* **2008**, *130*, 1568−1569.

https://dx.doi.org/10.1021/acsami.9b20231
ACS Appl. Mater. Interfaces 2020, 12, 9617−9627

(49) Wang, J.; Rao, P.; An, W.; Xu, J.; Men, Y. Boosting Photocatalytic Activity of Pd Decorated TiO_2 Nanocrystal with Exposed (001) Facets for Selective Alcohol Oxidations. *Appl. Catal. B: Environ.* **2016**, *195*, 141−148.
(50) Shiraishi, Y.; Tsukamoto, D.; Sugano, Y.; Shiro, A.; Ichikawa, S.; Tanaka, S.; Hirai, T. Platinum Nanoparticles Supported on Anatase Titanium Dioxide as Highly Active Catalysts for Aerobic Oxidation under Visible Light Irradiation. *ACS Catal.* **2012**, *2*, 1984−1992.
(51) Chen, Y.; Wang, Y.; Li, W.; Yang, Q.; Hou, Q.; Wei, L.; Liu, L.; Huang, F.; Ju, M. Enhancement of Photocatalytic Performance with the Use of Noble-Metal-Decorated TiO_2 Nanocrystals as Highly Active Catalysts for Aerobic Oxidation under Visible-Light Irradiation. *Appl. Catal. B: Environ.* **2017**, *210*, 352−367.
(52) Qian, K.; Sweeny, B. C.; Johnston-Peck, A. C.; Niu, W.; Graham, J. O.; DuChene, J. S.; Qiu, J.; Wang, Y.-C.; Engelhard, M. H.; Su, D.; Stach, E. A.; Wei, W. D. Surface Plasmon-Driven Water Reduction: Gold Nanoparticle Size Matters. *J. Am. Chem. Soc.* **2014**, *136*, 9842−9845.
(53) Liu, X.; Liu, M.-H.; Luo, Y.-C.; Mou, C.-Y.; Lin, S. D.; Cheng, H.; Chen, J.-M.; Lee, J.-F.; Lin, T.-S. Strong Metal-Support Interactions between Gold Nanoparticles and ZnO Nanorods in CO Oxidation. *J. Am. Chem. Soc.* **2012**, *134*, 10251−10258.
(54) Tang, H.; Su, Y.; Guo, Y.; Zhang, L.; Li, T.; Zang, K.; Liu, F.; Li, L.; Luo, J.; Qiao, B.; Wang, J. Oxidative strong metal-support interactions (OMSI) of supported platinum-group metal catalysts. *Chem. Sci.* **2018**, *9*, 6679−6684.
(55) Tauster, S. J.; Fung, S. C.; Garten, R. L. Strong Metal-Support Interactions. Group 8 Noble Metals Supported on Titanium Dioxide. *J. Am. Chem. Soc.* **1978**, *100*, 170−175.
(56) Qiao, B.; Wang, A.; Yang, X.; Allard, L. F.; Jiang, Z.; Cui, Y.; Liu, J.; Li, J.; Zhang, T. Single-Atom Catalysis of CO Oxidation Using Pt_1/FeO_x. *Nat. Chem.* **2011**, *3*, 634−641.
(57) Fu, Q.; Wagner, T.; Olliges, S.; Carstanjen, H.-D. Metal−Oxide Interfacial Reactions: Encapsulation of Pd on TiO_2 (110). *J. Phys. Chem. B* **2005**, *109*, 944−951.
(58) Wang, L.; Wang, H.; Rice, A. E.; Zhang, W.; Li, X.; Chen, M.; Meng, X.; Lewis, J. P.; Xiao, F.-S. Design and Preparation of Supported Au Catalyst with Enhanced Catalytic Activities by Rationally Positioning Au Nanoparticles on Anatase. *J. Phys. Chem. Lett.* **2015**, *6*, 2345−2349.
(59) Wang, Y.; Widmann, D.; Behm, R. J. Influence of TiO_2 Bulk Defects on CO Adsorption and CO Oxidation on Au/TiO_2: Electronic Metal−Support Interactions (EMSIs) in Supported Au Catalysts. *ACS Catal.* **2017**, *7*, 2339−2345.
(60) Sanjinés, R.; Tang, H.; Berger, H.; Gozzo, F.; Margaritondo, G.; Lévy, F. Electronic Structure of Anatase TiO_2 Oxide. *J. Appl. Phys.* **1994**, *75*, 2945−2951.
(61) Devadoss, A.; Kuragano, A.; Terashima, C.; Sudhagar, P.; Nakata, K.; Kondo, T.; Yuasa, M.; Fujishima, A. Single-Step Electrospun TiO_2−Au Hybrid Electrodes for High Selectivity Photoelectrocatalytic Glutathione Bioanalysis. *J. Mater. Chem. B* **2016**, *4*, 220−228.
(62) Gong, X.-Q.; Selloni, A.; Dulub, O.; Jacobson, P.; Diebold, U. Small Au and Pt Clusters at the Anatase TiO_2(101) Surface: Behavior at Terraces, Steps, and Surface Oxygen Vacancies. *J. Am. Chem. Soc.* **2008**, *130*, 370−381.
(63) Casaletto, M. P.; Longo, A.; Martorana, A.; Prestianni, A.; Venezia, A. M. XPS Study of Supported Gold Catalysts: the Role of Au^0 and $Au^{+\delta}$ Species as Active Sites. *Surf. Interface Anal.* **2006**, *38*, 215−218.
(64) Si, R.; Flytzani-Stephanopoulos, M. Shape and Crystal-Plane Effects of Nanoscale Ceria on the Activity of Au-CeO_2 Catalysts for the Water−Gas Shift Reaction. *Angew. Chem.* **2008**, *120*, 2926−2929.
(65) Priebe, J. B.; Karnahl, M.; Junge, H.; Beller, M.; Hollmann, D.; Brückner, A. Water Reduction with Visible Light: Synergy between Optical Transitions and Electron Transfer in Au-TiO_2 Catalysts Visualized by In situ EPR Spectroscopy. *Angew. Chem., Int. Ed.* **2013**, *52*, 11420−11424.
(66) Endrődi, B.; Kecsenovity, E.; Rajeshwar, K.; Janáky, C. One-Step Electrodeposition of Nanocrystalline TiO_2 Films with Enhanced Photoelectrochemical Performance and Charge Storage. *ACS Appl. Energy Mater.* **2018**, *1*, 851−858.
(67) Boccuzzi, F.; Chiorino, A.; Manzoli, M.; Andreeva, D.; Tabakova, T. FTIR Study of the Low-Temperature Water−Gas Shift Reaction on Au/Fe_2O_3 and Au/TiO_2 Catalysts. *J. Catal.* **1999**, *188*, 176−185.
(68) Boccuzzi, F.; Chiorino, A.; Manzoli, M. FTIR Study of the Electronic Effects of CO Adsorbed on Gold Nanoparticles Supported on Titania. *Surf. Sci.* **2000**, *454−456*, 942−946.
(69) Bian, Z.; Tachikawa, T.; Zhang, P.; Fujitsuka, M.; Majima, T. Au/TiO_2 Superstructure-Based Plasmonic Photocatalysts Exhibiting Efficient Charge Separation and Unprecedented Activity. *J. Am. Chem. Soc.* **2014**, *136*, 458−465.
(70) Subramanian, V.; Wolf, E.; Kamat, P. V. Semiconductor−Metal Composite Nanostructures. To What Extent Do Metal Nanoparticles Improve the Photocatalytic Activity of TiO_2 Films? *J. Phys. Chem. B* **2001**, *105*, 11439−11446.

https://dx.doi.org/10.1021/acsami.9b20231
ACS Appl. Mater. Interfaces 2020, 12, 9617−9627